catalysts

MDPI

Article

Preparation and Performance Evaluation of Cu-Ni Electrodes for Electrochemical Nitrate Reduction in an Undivided Cell

Maria Grazia Rubanu, Nicola Melis, Laura Mais, Michele Mascia and Annalisa Vacca *

Dipartimento di Ingegneria Meccanica, Chimica e dei Materiali, Università degli Studi di Cagliari, Via Marengo 2, 09123 Cagliari, Italy; mariag.rubanu@unica.it (M.G.R.); nicola.melis87@unica.it (N.M.); laura.mais@unica.it (L.M.); michele.mascia@unica.it (M.M.)

* Correspondence: annalisa.vacca@unica.it

Abstract

Cu-Ni co-deposit electrodes were prepared and tested in an undivided cell for the electrochemical removal of nitrate from aqueous solutions. Pulsed electrodeposition (PED) under a dynamic hydrogen bubble template and direct electrodeposition (DE) techniques were used for synthetizing porous nickel- and copper-based cathodes. Scanning electron microscopy (SEM) and energy dispersive X-ray (EDX) analyses showed dendritic and cauliflower-like deposits with a uniform distribution of nickel and copper on the electrode surface, both using flat and foam nickel supports. The PED technique on nickel foam generated highly porous Cu-Ni coatings, with the largest electrochemical active surface area (ECSA) among all the investigated electrodes. Electrolysis in alkaline solutions containing nitrates was performed in an undivided cell in potentiostatic mode. The selectivity towards N_2 was strongly dependent on both copper loading and applied potential; in particular, the foam electrode containing about 23% Cu showed very low ammonia production even at the highest cathodic overpotential, evidencing its marked preference for nitrogen formation. The process performed in the undivided cell using foam-supported Cu-Ni cathodes enabled 100% of conversion of nitrate to molecular nitrogen within approximately 7 h, allowing the complete denitrification of the water.

Keywords: nitrate electroreduction; nitrogen selectivity; electrochemical treatment; Cu-Ni bimetallic cathodes; pulsed electrodeposition (PED)

1. Introduction

Nitrates (NO_3^-) are the most thermodynamically stable oxidized form of nitrogen in aqueous systems and show high chemical endurance due to their strong N–O bonds and low reactivity under ambient conditions. An excess of nitrates can lead to the eutrophication of aquatic ecosystems and to a reduction in dissolved oxygen content. Industrial activities, ranging from pharmaceutical to textile, together with agricultural activities and soil leaching, contribute significantly to nitrate contamination of both surface water and groundwater. As a result, advanced denitrification processes must be implemented to effectively mitigate nitrate contamination and to meet the increasingly strict discharge limits imposed by environmental legislation.

The most applied methods for the denitrification process can be divided into physical, chemical and biological approaches. Physical processes, such as ammonia stripping, ion exchange and adsorption, are efficient at removing most pollutants, but they are expensive and could also generate secondary pollution that needs to be treated. Biological approaches,

Academic Editor: Guido Busca

Received: 15 June 2026
Revised: 10 July 2026
Accepted: 16 July 2026
Published: 18 July 2026

which require the use of anammox bacteria, achieve high degradation efficiencies without generating additional contaminants. However, they are energy-consuming, as they often need additional carbon resources. Chemical methods, such as magnesium ammonium phosphate hexahydrate (MAP) precipitation, lead to fast, simple and highly efficient denitrification of wastewater, but they require laboratory-intensive work as well as secondary treatment for complete removal [1]. In this context, electrochemical reduction has emerged as a particularly promising alternative to convert nitrate into high-value-added ammonia and remove NO_3^- pollution [2–4].

NO_3RR is a multistep process involving up to eight electrons depending on the final product and proceeds through several adsorbed intermediates such as nitrite (NO_2^-), nitric oxide (NO), nitrous oxide (N_2O), hydroxylamine (NH_2OH), ammonia (NH_3), and nitrogen (N_2) [5,6].

According to the Pourbaix diagram, nitrogen (N_2) and ammonia (NH_3) are the most thermodynamically stable species in the pH range 0–14, especially in drinking water (pH 6–9) [7,8]. Nitrite is the primary quasi-stable intermediate formed during the electrochemical reduction in nitrate before it is completely reduced to ammonia or nitrogen. Thus, the reduction in nitrate (NO_3^-) can be divided into two steps: the conversion of nitrate (NO_3^-) to nitrite (NO_2^-) and the conversion of nitrite (NO_2^-) to ammonia or nitrogen [9]. The rate-limiting step of the process is the conversion of nitrate to nitrite, which occurs after initial adsorption onto the cathode surface [10]. This step requires efficient adsorption of nitrate onto the cathode surface followed by electron transfer. Therefore, catalyst design and operating conditions must be carefully optimized to enhance nitrate conversion.

Nowadays, research efforts are increasingly directed towards ammonia production from nitrate wastes by the NO_3RR process, which is considered a potential alternative to the well-known Haber–Bosh process [11,12]. Among the emerging electrochemical strategies for ammonia synthesis, the nitrogen reduction reaction (NRR) and the nitric oxide reduction reaction (NORR) have also attracted significant attention due to their potential for sustainable nitrogen fixation and resource recovery [13,14]. However, when electrochemical treatment is proposed for the mitigation of the eutrophication phenomenon, the removal of all the reactive nitrogen, including ammonia, is preferred.

The selectivity of the process to form NH_3 or N_2 depends on different factors such as reaction conditions, catalyst composition, electrode structure and preparation method. At high current densities, the hydrogen evolution reaction (HER) competes with NO_3RR, lowering its faradaic efficiency [15,16]. Hence, identifying the optimal operative conditions is important to maximize the conversion of nitrates to nitrogen and to minimize the HER rate [17,18].

Although the NO_3RR can be carried out at any nitrate concentration, the reduction mechanism is strongly influenced by its concentration. At high nitrate concentration levels, an autocatalytic mechanism is initiated, which accelerates nitrate reduction and enhances faradaic efficiency [19,20]. Moreover, high nitrate concentrations can enhance the mass-transfer-limited adsorption of NO_3^- to the active site, constituting the first step of the reduction process [21,22].

NO_3RR can be enhanced at the electrode surface by adjusting electrolysis conditions (e.g., current density, potential, electrolysis duration), controlling process parameters (e.g., temperature, stirring speed, electrolyte flow rate), and modifying the electrode (e.g., electrodeposition, electrochemical redox treatments, surface functionalization or nano-structuring) [21,23]. As mentioned earlier, the preparation of an efficient cathode with a high electrocatalytic surface area is one of the main factors to improve the nitrate degradation rates.

The choice of the electrode material strongly influences both the kinetics and the product selectivity during the electrochemical nitrate reduction. Metals with highly filled *d*-orbitals and partially open *d*-shells—such as Cu, Ag, and Pt—are particularly suitable for this process [24]. Their *d*-orbital energy levels are similar to the π* LUMO of nitrate, promoting the initial electron transfer step. Among these, copper stands out for its excellent catalytic activity and low cost [25]. However, its practical use in the denitrification process is limited due to its low stability, mainly due to corrosion and metal leaching. Recent studies suggest that Cu-based deposits offer a promising solution by combining the desirable properties of multiple metals into a single electrode material.

Electrodeposited Cu-Ni materials have been previously investigated as cathodes for nitrate degradation, exhibiting high catalytic efficiencies in samples with higher copper content [26,27]. Copper sites promote the nitrate adsorption while nickel sites adsorb the hydrogen produced in alkaline or acidic conditions. Nickel promotes the hydrogenation of intermediates species such as NO_2^- accelerating their desorption and enhancing the kinetics and efficiency of NO_3RR [28].

Another key aspect of catalyst design is its selectivity towards nitrogen or ammonia formation. Zhu et al. reported the synthesis of nanocomposites of Cu and NiO as catalysts for the NO_3RR process, achieving faradaic efficiency of 97% for ammonia production [29]. The selectivity towards nitrogen formation is usually low, primarily due to the challenges associated with N−N bond coupling on the catalyst surfaces [17]. However, high selectivity for N_2 and complete nitrate removal have been achieved using iron nanoparticles in carbon microspheres (CL-Fe@C) [30] and iron-based nanofibers (Fe/NF_s) [31] as cathode coupled with Pt anode in an undivided cell: the combination of a low-cost cathode with an efficient anode such as Platinum may lead to the formation of harmless nitrogen [32].

In this framework, the aim of the present work is to investigate the electrochemical reduction in nitrates in an undivided electrochemical cell using electrodeposited Cu-Ni cathodes for denitrification purposes. The influence of catalyst composition, electrode structure and applied potential on the removal of nitrates and selectivity towards molecular nitrogen has been studied.

The electrochemical active surface area (ECSA) of the electrodes was determined from double layer capacitance values obtained by cyclic voltammetry and analyzed using the Trasatti method. This approach allowed us to distinguish the contribution of inner (diffusive) and outer (surface) capacitance, thereby correlating morphological features with catalytic performance. The characterization of the electrode/electrolyte interface was also carried out through electrochemical impedance spectroscopy (EIS), whose results are reported in the Supporting Information (Figure S2, Table S1).

In addition, scanning electron microscopy (SEM) and energy-dispersive X-ray (EDX) analyses were performed to correlate surface morphology, porosity, and elemental composition with the electrochemical behavior of the electrodes.

Finally, a kinetic analysis of the experimental results was conducted to provide mechanistic insight into the denitrification process and to identify the conditions that favor nitrogen formation in undivided cell configurations.

2. Results and Discussion

2.1. Preparation and Characterization of Cu-Ni and Ni Electrodes

In this work, two electrodeposition techniques were employed to synthetize nickel- and copper-based cathodes: pulsed electrodeposition (PED) and direct electrodeposition (DE). The depositions were done onto nickel disk (ND) and nickel foam (NF). Table 1 reports the experimental conditions adopted for the syntheses.

Table 1. Operative conditions used for the preparation of the Cu-Ni electrodeposits.

	Technique	Electrolyte	E_1 (V)	E_2 (V)	Deposition Surface
S_1	PED t_1 = 60 s t_2 = 3 s	$NiSO_4$ 0.1 M $CuSO_4$ 0.01 M H_3BO_3 0.1 M	−4.0	−0.5	ND
S_2	PED t_1 = 60 s t_2 = 3 s	$NiSO_4$ 0.1 M $CuSO_4$ 0.01 M H_3BO_3 0.1 M	−4.0	−0.5	NF
S_3	DE	$NiSO_4$ 0.1 M $CuSO_4$ 0.01 M H_3BO_3 0.1 M	−1.1	-	NF
S_4	DE	$NiSO_4$ 0.1 M H_3BO_3 0.1 M	−4.0	-	ND

Figure 1 presents the surface morphology of the obtained electrodeposits, together with representative EDX mapping images for samples S_2 and S_3. The corresponding atomic percentages (at%) of Cu and Ni, extrapolated from EDX analyses, are reported in Table 2. According to the literature, samples prepared using PED present a hierarchical structure, while the combination of PED with the dynamic hydrogen bubble template method produces highly porous electrodes [27]. Sample S_1, prepared by PED, exhibits a hierarchical macroporous structure with a typical dendritic pattern. This morphology is consistent with previous reports by Hao et al. for the synthesis of highly porous Ni catalysts for OER applications in alkaline media [33]. The same morphology is described by Sengupta et al. for the preparation of nickel electrodeposits under HER conditions and high voltages [34]. According to their works, the dendritic morphology observed is related to the voltage applied (E_1 = −4 V). At this voltage, the HER is very fast; thus, the nickel and copper electrodeposition goes under a controlled-diffusion regime. Under these conditions, the deposition rate is limited by the diffusion of metal ions, resulting in non-uniform growth.

Sample S_2, also obtained by PED but on nickel foam (NF) support, presents a cauliflower-like structure that was also observed by Jituri et al. for the synthesis of nickel-manganese layered double hydroxide (NiMn-LDH) on porous nickel foam [35].

Previous studies showed that this characteristic morphology is due to the combination of the electrochemical deposition process and the hydrogen evolution reaction. The hydrogen bubbles alter the ionic concentration near the electrode surface, which affects the rate of the metal deposition in certain regions, causing them to grow faster than others. Also, the detachment of bubbles from the electrode surface leads to local discontinuity in the deposition process that creates a fractal-like growth [36].

Based on the atomic percentages obtained from the EDX mapping images reported in Table 2, S_2 presents a higher Cu content compared to S_1. This difference could be related to the different support used during pulsed electrodeposition: the three-dimensional and highly porous architecture of the nickel foam facilitates enhanced ion accessibility and localized deposition. S_3 was prepared by direct electrodeposition (DE): since the only parameter tunable in DE is the working potential (or current), the operational conditions for the preparation of sample S_3 were set up by choosing the optimal potential for both nickel and copper electrodeposition [34,37]. As sample S_2 (Figure 1B), S_3 (Figure 1C) presents a cauliflower-like structure [38]. S_2 (Figure 1E) exhibits a porous 3D structure where the pore walls are not closely packed, thus enhancing further the surface area [35,39]. S_3 (Figure 1F) shows a more uniform nickel and copper distribution than S_2 on the foam surface with densely deposited areas spread across it and a higher Cu percentage as well (Table 2). The

comparison between S_2 and S_3 clearly indicates that the deposition technique strongly influences the final composition: PED tends to produce Ni-rich deposits with less uniform Cu distribution, while DE favors copper incorporation and yields a more homogeneous coating. These differences in Cu/Ni ratio and spatial distribution are expected to play a decisive role in the electrocatalytic performance of the electrodes.

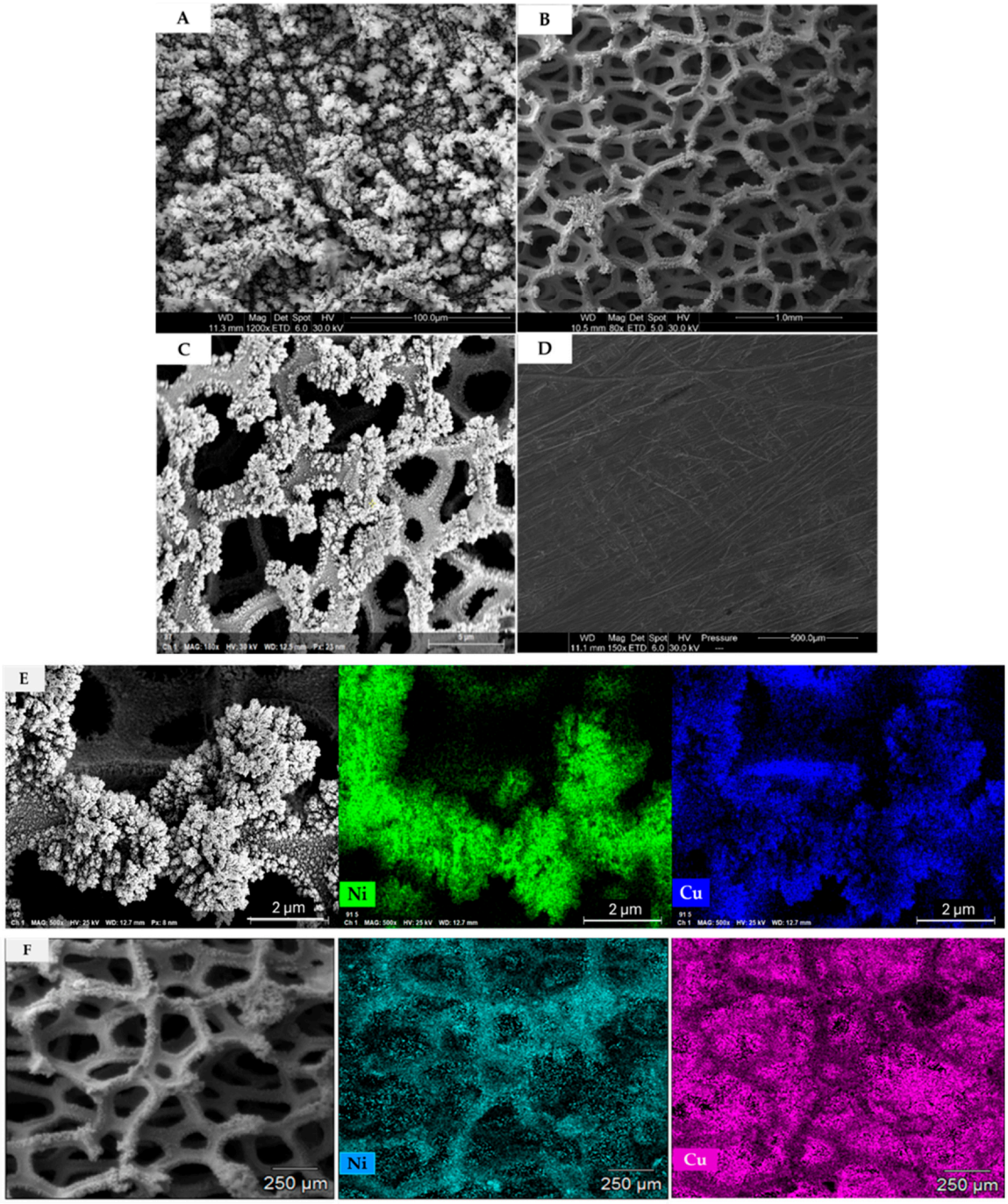

Figure 1. SEM mapping images of Cu-Ni and Ni electrodeposits: (**A**) sample S_1, (**B**) sample S_2, (**C**) sample S_3 and (**D**) sample S_4. EDX image of (**E**) sample S_2 and (**F**) sample S_3 that shows the Cu and Ni distribution onto the surface.

To elucidate the effect of the different compositions and structures of the electrodes, the electrochemically active surface area (ECSA) was determined from the double layer capacitance obtained through the CV method. The cyclic voltammograms were recorded in

the region of the open circuit potential (OCP) ± 0.05 V (vs. SCE) at high and low scan rates v, the last one being the region where the current response should be only related to the charging of the double layer. The capacitance of the samples was calculated with the Trasatti analysis that considers the contribution of an inner (diffusive) C_{dif} and outer (surface) capacitance C_{DL} to the overall capacitance C_{tot} according to the following equation:

$$C_{tot} = C_{dif} + C_{DL} \quad (1)$$

Assuming a semi-infinite linear diffusion, the total capacitance can be evaluated by plotting the reciprocal of the measured capacitance vs. the square root of the scan rate (Equation (2)), extrapolating the intercept for $v^{1/2} \rightarrow 0$ (see Figure 2A,C). In the same way, the outer capacitance can be evaluated by extrapolating the capacitance as a function of $v^{1/2}$ (Equation (3)) for $v \rightarrow \infty$ (see Figure 2B,D) [40–42].

$$\frac{1}{C(v)} = av^{\frac{1}{2}} + \frac{1}{C_{tot}} \quad (2)$$

$$C(v) = bv^{-\frac{1}{2}} + C_{DL} \quad (3)$$

However, deviation from linearity was observed at high scan rates in Figure 2B–D. This can be related to ohmic drops and permanent redox changes as a result of the electrode material's resistance. Therefore, the fitting was applied only to the data points that are close to the nearly linear region [43,44].

Table 2. Atomic percentages of Cu and Ni onto the surface of S_1–S_4.

	Composition in at (%)
S_1	$Cu_{14}Ni_{86}$
S_2	$Cu_{23}Ni_{77}$
S_3	$Cu_{58}Ni_{42}$
S_4	Cu_0Ni_{100}

Table 3 reports the values of C_{tot} and C_{DL} obtained from the Trasatti plots together with the contribution of diffusion (C_{dif}) calculated by Equation (1). Coherently with the SEM images, sample S_2 showed the highest values of capacitance; this result confirmed that the enhanced surface morphology and porosity of S_2 provided a larger electrochemically active area, leading to a predominant diffusional contribution to the overall capacitance. Moreover, deposits on nickel foam presented a very high diffusional capacitance, being the main contribution to the overall capacitance.

The electrochemical active surface area (ECSA) was calculated by normalizing the C_{DL} values of the samples to that of a smooth Ni electrode [33], which is 0.02 mF cm^{-2} and by considering the geometric area, as follows:

$$ECSA = \frac{C_{DL}(S_x)}{C_{DL}(ND)} \times A_{geometric} \quad (4)$$

Among all the Cu-Ni disks, S_1 exhibited an electrochemical surface area (ECSA) four times larger than that of S_4, confirming the beneficial effect of copper on the enhancement of the electrocatalytic area [21,30,45]. Among the foams, S_2 showed a higher ECSA value than S_3, and this could be related to the different electrodeposition techniques used for their preparation. For both samples, the intrinsic porosity of the nickel foam contributed significantly to the measured ECSA and C_{DL}, as confirmed by the values obtained for the bare NF using the Trasatti method (ECSA = 166.27 cm^2 and C_{DL} = 2.55 mF cm^{-2}).

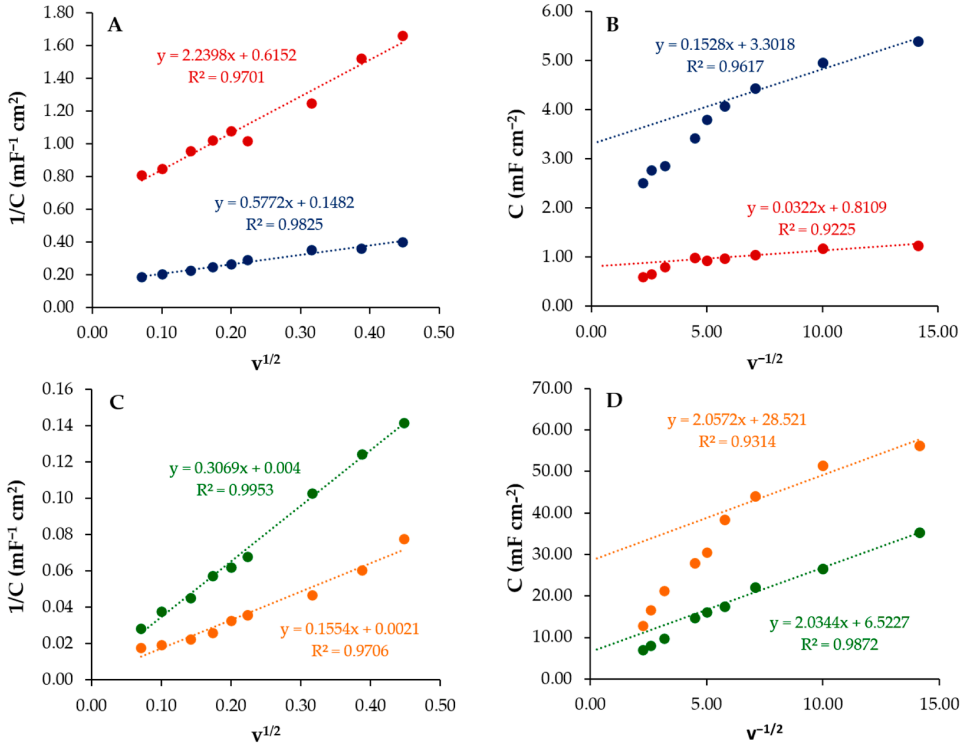

Figure 2. Evaluation of the capacitance contribution with the Trasatti method: (**A**–**C**) Plots of the reciprocal of capacitance vs. the square root of the scan rate and (**B**–**D**) Plots of capacitance vs. reciprocal of square root of scan rate for each sample: S_1 (blue symbols); S_2 (orange symbols); S_3 (green symbols); S_4 (red symbols).

Table 3. Electrochemical parameters of samples S_1–S_4, including total capacitance (C_{tot}), double-layer capacitance (C_{DL}), diffusion-related capacitance (C_{diff}), electrochemically active surface area (ECSA), and the relative contributions of C_{DL} and C_{diff} to C_{tot}.

	C_{total} (mF cm^{-2})	C_{DL} (mF cm^{-2})	C_{diff} (mF cm^{-2})	ECSA (cm^2)	C_{DL}/C_{tot} (%)	C_{dif}/C_{tot} (%)
S_1	6.7	3.3	3.4	129.6	48.93	51.07
S_2	476.2	28.5	447.7	1939.4	5.99	94.01
S_3	250.0	6.5	243.5	1108.7	2.61	97.39
S_4	1.6	0.8	0.81	31.8	49.83	50.17

2.2. Assessment of Catalysts' Activity for the NO_3RR Process

To study the catalytic behavior of the obtained samples, linear sweep voltammetries were performed for all samples at a scan rate of 0.5 mV s^{-1}, starting from the open circuit potential to a cathodic potential of E = −1.6 V (vs. SCE), either in a solution of KOH (1 M) or in KNO_3 (0.1 M)/KOH (1 M) used as a synthetic electrolyte for the denitrification process. The current densities, normalized with the electrochemical active surface area (ECSA), are plotted against E (vs. SCE) and the graphs are presented in Figure 3. For clarity, two pairs of curves were presented in Figure 3A (deposits on nickel disks) and Figure 3B (deposits on nickel foams) measured in the presence of nitrate ions (full line) and in their absence (dashed line). As can be observed in Figure 3, the presence of nitrate in solution determines an increase in the cathodic current density for samples S_1, S_2 and S_3, confirming their electrocatalytic activity towards the nitrate reduction. In contrast, in the case of sample S_4, which was synthesized without copper, no current enhancement was observed in the presence of nitrate, indicating that the presence of copper in the deposits

is essential to achieve good catalytic performance towards nitrate reduction. Moreover, for copper-containing samples, the current onset in the presence of nitrates is shifted to lower cathodic potentials as the copper content in the deposits increases, with the most pronounced effect observed for S_3.

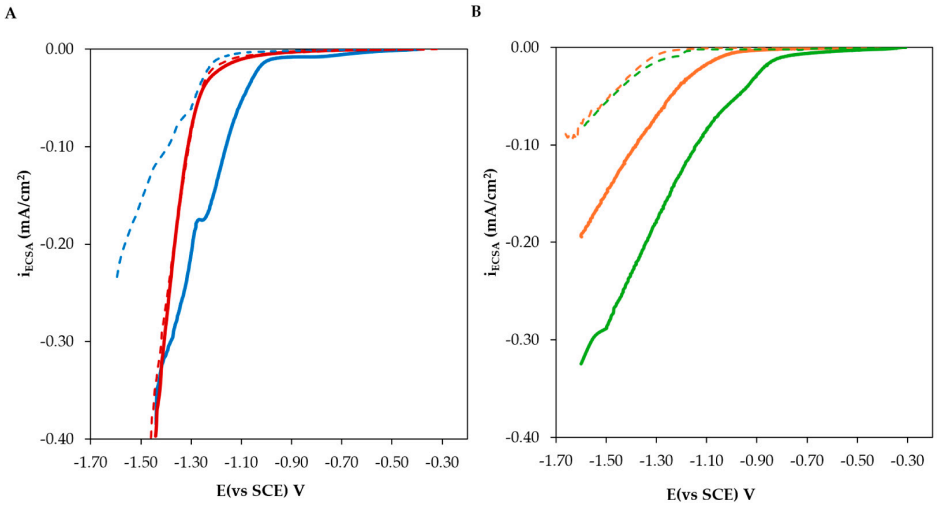

Figure 3. ECSA-normalized LSV plots. (**A**) Sample S_1 (blue curves) and sample S_4 (red curves); (**B**) sample S_2 (orange curves) and sample S_3 (green curves). Dashed lines refer to KOH 1 M; full lines refer to KOH 1 M and KNO_3 0.1 M.

To gain insights on the NO_3RR, Tafel analysis was carried out on the linear sweep voltammetry measurements in KOH/KNO_3 (full lines) and in KOH (dashed lines) shown in Figure 3. The main parameters extrapolated from the Tafel study were the overpotential (η) and the exchange current density (J_0) as well as the Tafel slope (Table 4). The kinetic parameters were determined by considering both the geometric area of the electrodes and ECSA. The polarization curves are described by the Tafel equation:

$$\eta = a + b\log j \quad (5)$$

where η is the overpotential, b is the Tafel slope, j is the current density, and a is the intercept of the curve, which is related to the exchange current density J_0 through the equation:

$$a = \frac{2.3RT}{\beta nF} \times \log(J_0) \quad (6)$$

Table 4. Kinetic parameters of samples S_1–S_4. The overpotential η (mV) was calculated at a current density of 10 mA/cm^2.

Sample	ECSA (cm^2)	Electrolyte	b ($mV\ dec^{-1}$)	$J_{0(Geometric)}$ ($mA\ cm^{-2}$)	$J_{0(ECSA)}$ ($mA\ cm^{-2}$)	$\eta_{10(Geometric)}$ (mV)
S_1	129.6	KOH/KNO_3	169.4	4.22	2.55×10^{-2}	61.3
		KOH	442.4	0.46	2.78×10^{-3}	234.5
S_2	1939.4	KOH/KNO_3	219.2	10.74	8.86×10^{-3}	31.7
		KOH	191.5	3.39	2.79×10^{-3}	493.1
S_3	1108.7	KOH/KNO_3	366.2	36.37	1.12×10^{-1}	405.8
		KOH	346.8	62.0	1.90×10^{-1}	n.d.
S_4	31.8	KOH/KNO_3	345.4	0.13	3.21×10^{-3}	412.2
		KOH	259.86	0.16	3.95×10^{-3}	448.5

S_1 and S_2 exhibited the lowest Tafel slope (169.4 mV dec^{-2} and 219.2 mV dec^{-2}) in the presence of nitrate, suggesting faster reaction kinetics compared to the other electrodes as well as lower overpotential values together with a relatively high exchange current density. S_3 presented the highest exchange current density; however, it requires a much higher overpotential compared to S_1 and S_2. As expected, S_4 showed comparatively poor catalytic performance, characterized by a high overpotential (412.2 mV) and a very low exchange current density. According to the previous literature, a Tafel slope close to 120 mV dec^{-1} is indicative of NO_3^- conversion to NO_2^- as an intermediate [46–49]. Higher Tafel slopes usually indicate that NO_3RR is hindered by the initial adsorption and activation of NO_3^- [50]. Although S_1 presented the closest value to 120 mV dec^{-1}, in this study NO_2^- was not detected because it might have been consumed more rapidly in the undivided cell. The comparison between the Tafel results, extrapolated from the LSV measurements that were carried out in KOH/KNO_3 and in KOH, clearly indicates the significant impact that HER has on the electrodes' catalytic efficiency towards NO_3RR. Sample S_3 exhibits a higher exchange current density for HER together with the highest current densities recorded at all potentials (Figure S1). These elements may impact the overall reaction environment by facilitating the hydrogen availability at the catalyst surface, and that may explain the tendency of S_3 toward ammonia production as shown in Figure 4.

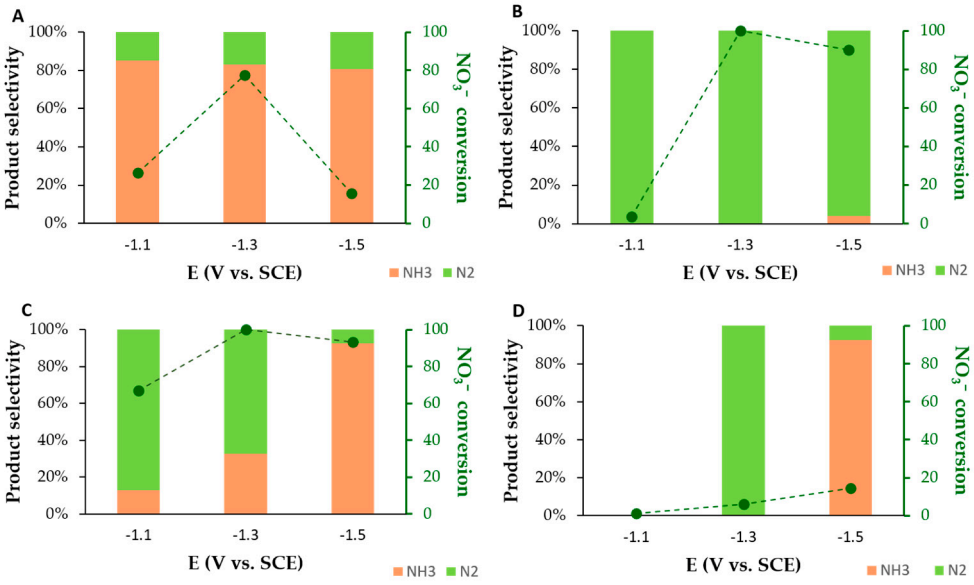

Figure 4. Investigation on the product selectivity (%) and nitrate conversion (%) during the NO_3RR (7 h) at three reduction potential E (vs. SCE) = −1.1 V, −1.3 V, −1.5 V for samples S_1 (**A**), S_2 (**B**), S_3 (**C**), S_4 (**D**).

Electrochemical impedance spectroscopy (EIS) was also performed to further characterize the samples investigated. As an example, the Nyquist plot of S_3 is reported in the Supporting Information, along with the fitted parameters interpreted using the equivalent circuit shown in Figure S2. The circuit consists of the solution resistance (R_s), a charge-transfer resistance (R_{ct}), two constant-phase elements associated with the double-layer (C_{DL}) and diffusive (C_{dif}) contributions, together with the corresponding diffusive resistance (R_{dif}). The impedance parameters (Table S1) are fully consistent with the morphological and capacitive trends previously discussed. Samples containing copper exhibit markedly lower R_{ct} values compared to bare nickel, confirming the beneficial role of Cu sites in promoting nitrate adsorption and electron transfer. In particular, S_2 and S_3 show the smallest R_{ct} (0.17 and 0.18 Ω, respectively), in agreement with their high ECSA and porous architecture. Conversely, S_4 displays a much larger R_{ct} (77.14 Ω), reflecting its poor

catalytic performance toward nitrate reduction, according to the current density exchange values. The diffusive resistance (R_{dif}) also highlights the strong influence of electrode structure: foam-supported Cu-Ni electrodes exhibit significantly lower R_{dif} than S_1 and S_4, confirming that hierarchical porosity and 3D architecture facilitate mass transport and reduce the diffusional limitations typically associated with nitrate reduction.

As discussed earlier, Figure 3A,B shows that the current response recorded for all samples in the presence of KNO_3 (0.1 M)/KOH (1 M) can be attributed to the electrochemical activity associated with the nitrate species. Based on these observations, a range of potentials was selected to perform the denitrification study under potentiostatic conditions, following the approach proposed by Shish et al. [51], whose Cu-Ni electrodes achieved a complete nitrate removal within 5 h. As previously discussed, the denitrification process often competes with the hydrogen evolution reaction under cathodic conditions. At more negative potentials, HER tends to dominate due to its favorable kinetics, thereby hindering nitrate reduction by subtracting electrons from the desired denitrification pathway. Consequently, the overall efficiency of nitrate degradation can be reduced. The extent of this competition is affected by several factors such as electrode material, surface morphology, and pH that can selectively promote one reaction pathway over the other [21,23,52]. The denitrification process was carried out with the four investigated samples under potentiostatic conditions at three potentials of −1.1 V, −1.3 V and −1.5 V vs. SCE, selected according to Figure 3A,B as from −1.0 V a current ascribed to NO_3RR was detected. The lower potential value corresponds to the onset of NO_3RR, while the highest corresponds to the fully developed HER.

The trends with time of the current densities are reported in Figure S1; in the early stage a rapid decrease in current density is observed, followed by a stable trend towards less cathodic current as nitrate is progressively depleted from the solution. Current fluctuations, particularly at the beginning of the experiment, may be associated with local bubble formation/detachment, while current spikes visible at fixed times are related to the withdrawal of the samples. Figure S1 also reports the chronoamperometric measurement normalized by the ECSA. It can be noticed that the highest values of current densities have been obtained for sample S_3, confirming its superior intrinsic catalytic activity.

It is well known that nitrate reduction can proceed through several intermediate nitrogen-containing species, including NO, N_2O, NO_2^-, NH_2OH, and other transient products, depending on the reaction conditions and catalyst. In alkaline media, these intermediates may undergo further reduction or decomposition, ultimately yielding the thermodynamically stable end products N_2 and NH_3/NH_4^+.

The results obtained in this work showed that, under all these tested conditions, NH_3 was the only by-product directly detected for every sample, whereas the production of N_2 was determined from the mass-balance relationship. Less stable gaseous nitrogen compounds, such as NO and N_2O, were not considered in the present work [51,53,54]. Figure 4 reports both the selectivity of the process and nitrate conversion during the NO_3RR after 7 h of treatment under the three applied cathodic potentials. As can be seen, sample S_2 presents, for all the selected potentials, the highest conversions of nitrate to nitrogen and can therefore be identified as N_2-selective electrocatalyst. For samples S_3 (Figure 4C) and S_4 (Figure 4D), the selectivity towards N_2 decreases with increasing applied potential, leading to higher amounts of ammonia production. This behavior can be explained by considering the predominance of the hydrogen evolution reaction at more negative potentials, which favors the ammonia formation as a hydrogenated reduction product. The highest conversion of nitrate was obtained at −1.3 V for the samples containing copper, while the nickel sample always showed very low conversion of nitrates,

being zero at −1.1 V, underlining the central role that copper has in the denitrification process [55–58].

It is important to note that the electrochemical cell used in this work is undivided; thus, the concurrent reactions happening at the anode must be considered. Under the operative conditions adopted in the present work, the oxidation of NH_3, produced at the cathode during the NO_3RR, also occurs at the anode in the undivided cell, thereby contributing to the overall denitrification pathway through the further transformation of nitrogen intermediates. As evidenced by Polatides and Kyriacou, higher selectivity of the denitrification process towards nitrogen can be obtained in an undivided cell, while, in a divided cell, the process is more selective towards ammonia [59]. Since the purpose of this work is the complete removal of nitrates, the use of an undivided cell helps to achieve the result. Figure 5 shows the trends with time of nitrate, ammonia and nitrogen obtained during the electrolysis at the optimal working potential for all samples, which is −1.3 V as established from the results reported in Figure 5. As can be seen, the trend with time of ammonia is characterized by an initial build-up, reaching a maximum concentration at intermediate reaction times, followed by a progressive decline. This behavior is consistent with the formation of ammonia at the cathode and the subsequent consumption at the anode.

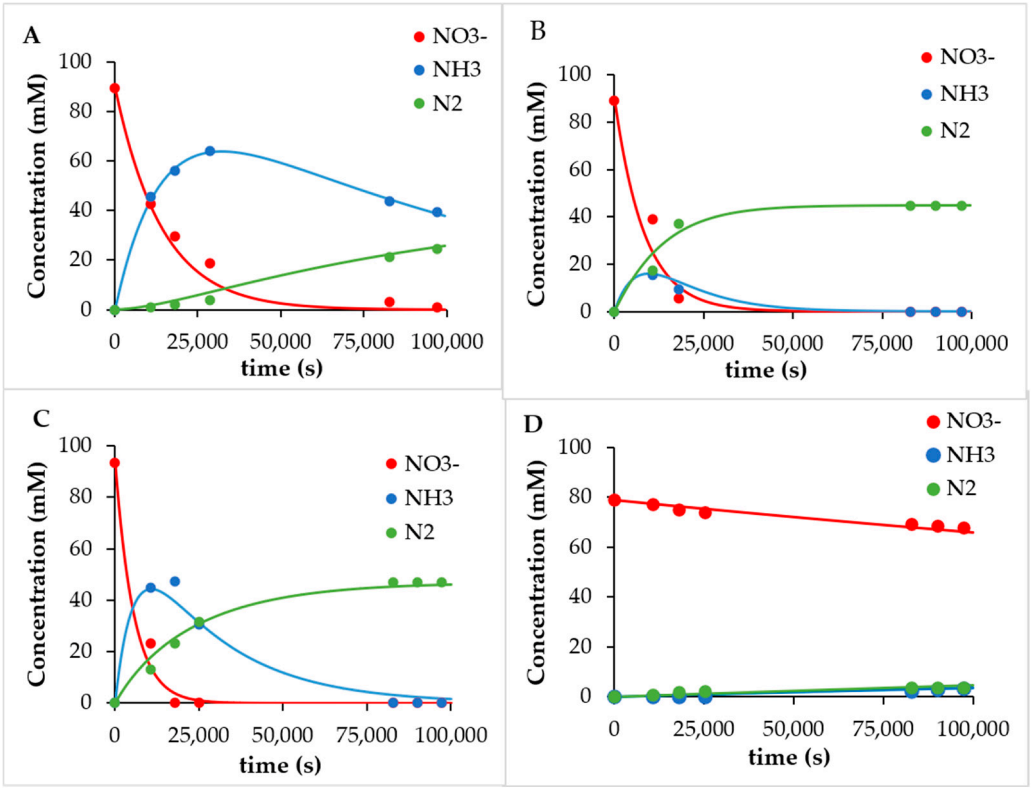

Figure 5. Trend with time of experimental (dots) and model-predicted data (lines) of nitrate, ammonia and nitrogen concentrations during the electrolysis at E (vs. SCE) = −1.3 V for samples S_1 (**A**), S_2 (**B**), S_3 (**C**) and S_4 (**D**).

2.3. Kinetic Analysis of the Catalyst in an Undivided Cell

As can be seen, for the electrodes containing copper, ammonia is produced from the very initial time of treatment, and it shows a maximum indicating the presence of its oxidation to form nitrogen. Moreover, nitrogen is also formed from the early stage of the process, specifically for the foam-supported electrodes, indicating a parallel cathodic reduction in nitrate to nitrogen. Based on the observed trends with time of NO_3^-, NH_3 and N_2 the main reactions occurring in the electrolytic cell are described below.

At the cathode:

$$NO_3^- + 6H_2O + 8e^- \rightarrow NH_3 + 9OH^- \quad (7)$$

$$NO_3^- + 3H_2O + 5e^- \rightarrow \frac{1}{2}N_2 + 6OH^- \quad (8)$$

$$2H_2O + 2e^- \rightarrow H_2 + 2OH^- \quad (9)$$

At the anode:

$$NH_3 + 3OH^- \rightarrow \frac{1}{2}N_2 + 3H_2O + 3e^- \quad (10)$$

$$2OH^- \rightarrow H_2O + \frac{1}{2}O_2 + 2e^- \quad (11)$$

The following reaction mechanism in the undivided cell can be sketched:

$$NO_3^- \xrightarrow{k_1} NH_3 \xrightarrow{k_3} \frac{1}{2}N_2 \quad (12)$$

$$NO_3^- \xrightarrow{k_2} \frac{1}{2}N_2 \quad (13)$$

where k_1 and k_2 are the rate constants for the cathodic reduction from nitrate to ammonia and nitrogen, corresponding to cathodic Reactions (7) and (8), respectively, and k_3 is the rate constant for the ammonia oxidation, which corresponds to anodic Reaction (10).

The differential equations describing the phenomena involved are

$$\frac{d[NO_3^-]}{dt} = -k_1[NO_3^-] - k_2[NO_3^-] \quad (14)$$

$$\frac{d[NH_3]}{dt} = k_1[NO_3^-] - k_3[NH_3] \quad (15)$$

$$\frac{d[N_2]}{dt} = \frac{1}{2}k_2[NO_3^-] + \frac{1}{2}k_3[NH_3] \quad (16)$$

The system of Equations (14)–(16) was solved, and the numerical solution can be viewed in Figure 5 for data obtained at −1.3 V. The results of modeling under all the experimental conditions are reported in Figures S3 and S4. Good agreement with the experimental data was obtained, and the relevant kinetic constants were reported in Table 5.

Table 5. Rate constants obtained by fitting the experimental data with Equations (14)–(16) and faradaic efficiency values for the NO_3RR at 50% of nitrate conversion.

Sample	E (V vs. SCE)	$k_1 \times 10^5$ s^{-1}	$k_2 \times 10^5$ s^{-1}	$k_3 \times 10^5$ s^{-1}	h_{50}
S_1	−1.1	1.1	0.009	1.0	85%
	−1.3	6.9	0.1	1.1	73%
	−1.5	0.6	0.1	1.2	10%
S_2	−1.1	0.03	0.05	2.9	1%
	−1.3	5.0	7.1	9.1	50%
	−1.5	3.5	6.1	9.9	40%
S_3	−1.1	1.3	4.0	4.2	38%
	−1.3	13.0	5.1	4.1	58%
	−1.5	9.0	6.2	7.0	20%
S_4	−1.3	0.05	0.13	0.11	10%
	−1.5	0.65	0.01	1.5	3%

Values of faradaic yield reported in Table 5 have been calculated from the ratio between the charge associated with Reactions (7) and (8) (Q_{NO3}) and the supplied charge (Q_{tot}). The

charge Q_{NO3} has been evaluated by integrating the relevant current over time. The currents can be in turn obtained from the reaction rate (Equation (14)) and the Faraday law. The faradaic yields (h) have been calculated as

$$\eta_{NO_3^-} = \frac{Q_{NO_3^-}}{Q_{tot}} = \frac{C^0 VF}{Q_{tot}}\left[1 - 8{\cdot}e^{-k_1 t} - 5{\cdot}e^{-k_2 t}\right] \quad (17)$$

As can be observed, S_1 showed higher Faradaic efficiencies than the nickel foams modified. This observation can suggest that, despite their high surface area, S_2 and S_3 may not utilize their entire surface for the target nitrate reduction process due to the complex porous structure and the possible inhomogeneities of the deposit.

From the values of rate constants reported in Table 5, it can be observed that the effect of the different values of ECSA is that samples prepared on Ni foam support present higher values of k_1 and k_2 respect to those prepared on flat Ni. High kinetic constants for the conversion of nitrate to ammonia were observed for samples containing copper; sample S_3 (58%$_{at}$ Cu) presented the highest value for k_1 at −1.3 V. It is interesting to note that for S_3 at −1.1 V the value of k_2 is about three-fold higher than k_1, which indicates high selectivity of this electrode towards nitrogen with respect to ammonia at this potential. Sample S_2, which presents the highest ECSA and 23%$_{at}$ Cu shows values of k_2 higher than k_1 for all the applied potential, indicating its high ability to convert nitrate ions directly to nitrogen, with no build-up of ammonia. Sample S_4 shows low electrocatalytic activity for the denitrification process, as it tends to promote the HER, especially at more negative potentials. Moreover, the rate constants for the oxidation of ammonia to nitrogen (k_3) are comparable to k_1 and k_2, indicating that the anodic contribution is significant under all the experimental conditions adopted. With the flat S_1 electrode, k_3 only slightly varies with the potential, indicating that the mass transfer of NH_3 towards the anodic surface is the prevalent mechanism of ammonia anodic oxidation. In contrast, the nickel foam-supported electrodes (S_2 and S_3) show that the kinetic constant for ammonia anodic oxidation increases as the cathodic potential becomes more negative. The increase in the apparent kinetic constant under more cathodic polarization is that the increase in total current more than compensates for the concomitant decrease in Faradaic efficiency. Although a larger fraction of the current is diverted toward parasitic reactions at higher cathodic overpotentials, the absolute current driving ammonia oxidation still increases, leading to an overall enhancement of the measured reaction rate.

3. Materials and Methods

3.1. Chemicals and Materials

Nickel sulphate anhydrous ($NiSO_4$), copper sulphate hexahydrate ($CuSO_4{\cdot}6H_2O$), potassium hydroxide (KOH), potassium nitrate (KNO_3), sodium hydrogen carbonate ($NaHCO_3$) and sodium carbonate (Na_2CO_3) were supplied by Carlo Erba reagents S.r.l. (Cornaredo, Milano, Italy). Boric acid (H_3BO_3), hydrochloric acid (HCl) and Nessler's reagent were purchased from Sigma-Aldrich S.r.l. (Milano, Italy). All electrochemical experiments were performed at room temperature using a potentiostat/galvanostat (Bi-ologic VSP-3e, Seyssinet-Pariset, France) powered by Ec-lab software V11.60. Cu-Ni and Ni electrodeposits were prepared using, as support, either nickel disks (d = 1 cm, thickness = 0.25 mm, 99.8%, Sigma Aldrich Chemie, GmbH (Schnelldorf, Germany) or nickel foam (thickness 0.9 mm, 99.5%, GoodFellow Ltd., Huntingdon, UK).

3.2. Synthesis of Cu-Ni and Ni Electrodeposits

The electrochemical depositions onto nickel disks (S_1, S_4 = 0.785 cm^2) were carried out in a cylindrical custom-designed three-electrode cell realized by Teflon, in which the

working electrode was located at the bottom of the cell, with an aluminum disk used as electrical contact; a Pt grid, placed in front of the anode at 1 cm distance, and a saturated calomel electrode (SCE) were used as counter and reference electrodes, respectively. The electrodeposition onto nickel foams (S_2 = 1.36 cm^2; S_3 = 3.4 cm^2), was performed in a three-electrode beaker cell equipped with the working and counter electrodes (Pt grid) placed vertically and distanced by 3 cm, and a SCE that served as a reference electrode. Cu-Ni electrodeposition was performed using a solution containing $NiSO_4$ 0.1 M, $CuSO_4$*$6H_2O$ 0.01 M and H_3BO_3 0.1 M (pH = 4). Meanwhile, the Ni electrodeposit was prepared using $NiSO_4$ 0.1 M and H_3BO_3 0.1 M solutions. Pulsed electrodeposition (PED) and direct electrodeposition (DE) techniques were used for the synthesis of the electrodes. Specifically, samples S_1 and S_4 were prepared using a nickel disk (ND) as support, whereas samples S_2 and S_3 were obtained on a nickel foam (NF) to evaluate both the effect of Cu-Ni composition and the influence of catalyst morphology on the denitrification process. S_1 and S_2 were synthesized using a pulsed electrodeposition (PED) technique under the dynamic hydrogen bubble template (DHBT) method [34]. Hydrogen bubbles, generated as a side reaction during metal deposition under high voltages, act as dynamic templates; consequently, the resulting morphology of the sample depends on the interplay between metal electrocrystallization and the hydrogen evolution reaction [60]. The pulsed electrodeposition (PED) technique was employed alternating two potentials: E_1 (vs. SCE) = −4.0 V for 60 s, favoring nickel deposition and E_2 (vs. SCE) = −0.5 V for 3 s, promoting copper deposition. Pulses were repeated cyclically for a total deposition time of 90 min. Sample S_3 was prepared by direct electrodeposition (DE) at E (vs. SCE) = −1.1 V for the same duration [45]. Finally, an additional Ni electrodeposit was prepared via direct electrodeposition and under DHBT conditions at E (vs. SCE) = −4.0 V, using the same electrolyte but without copper, to provide a reference system for comparison with the Cu-Ni electrodes.

The morphology and chemical composition of the synthetized samples were investigated by scanning electron microscopy and energy dispersive x-ray map images, performed with Environmental scanning electron microscopy (ESEM) FEI Quanta 200 (FEI, Hillsboro, OR, USA) and with Coxem EM40 (Coxem, Daejeon, Republic of Korea) equipped with a probe Bruker Quantax ED-XS (Quantax, Billerica, MA, USA).

Cyclic voltammetry measurements were carried out in KOH 1 M at different scan rates (ranging from 5 mV s^{-1} to 200 mV s^{-1}) with a narrow potential window to determine the electrochemical capacitance of the synthetized samples. The capacitive and pseudocapacitive contributions of the electrode materials were quantitatively evaluated by applying the Trasatti method. Specifically, the total charge (q) obtained from the voltammetric response is plotted as a function of the reciprocal square root of the scan rate ($v^{-1/2}$), to evaluate the capacitive contribution of electrical double-layer capacitance (surface-controlled charge component) and the pseudocapacitive (diffusion-controlled charge component) reaction of electrode materials. Linear sweep voltammetries were performed from the open circuit potential (OCP) to −1.6 V (vs. SCE) in KOH 1 M with and without KNO_3 0.1 M with a scan rate of 0.5 mV s^{-1} for the selection of the working potentials for the NO_3RR.

3.3. Denitrification Experiments

The denitrification experiments were performed using an alkaline solution of KOH (1 M) in the presence of KNO_3 0.1 M as a source of nitrate. The experiments were performed in an undivided three-electrode cell under batch conditions. The cell consisted of a 25 cm^3 stirred glass tank immersed in a thermostatic bath at 25 ± 2 °C. The prepared materials were used as cathodes, platinised titanium grids placed in front of the cathode at a 1 cm distance, and a saturated calomel electrode (SCE) was used as a counter and reference electrode, respectively. The volume of the treated solution was 20 cm^3. Chronoamperometric

tests at three different potential values (−1.1 V, −1.3 V and −1.5 V vs. SCE) were performed for 24 h under continuous stirring; during the runs, at regular intervals of time, 20–50 mL of samples were withdrawn and analyzed to determine the ionic compositions. The concentration of relevant ions (nitrate, nitrite) was measured by suppressed conductivity ionic chromatography (IC, Shimadzu, Kyoto, Japan) equipped with a conductivity detector (CDD-10A VP), autosampler (SIL-20 AC), pump (LC-20 AD) and column oven (CTO-40S). A Metrosep Anion supp 5–250/4.0 column was used to detect the anions present in the samples; the mobile phase was 2.4 mM $NaHCO_3$/2 mM Na_2CO_3, flow rate 0.8 mL min^{-1}. Nessler's reagent was used to quantify the concentration of produced NH_3/NH_4^+. Standard solutions of NH_4Cl (0–20 ppm) were prepared. Moreover, 1 mL of the Nessler's reagent was added to 50 mL of each standard solution, and the absorbance was read at a wavelength of λ = 420 nm.

4. Conclusions

In this work, highly porous bimetallic copper–nickel (Cu-Ni) electrodes were successfully prepared via different electrodeposition techniques onto nickel disk and foam supports. The physicochemical and electrochemical characterizations showed that all Cu-Ni samples presented high electrocatalytic areas (ECSA), with S_2 and S_3 exhibiting the greatest values due to their inherent 3D-porous structures and the higher Cu deposition ratio. Electrochemical reduction experiments of NO_3^-, that were carried out at different potentials, showed that a complete removal of NO_3^- could be achieved in approximately 7 h with samples S_2 and S_3. This work shows that the overall efficiency of NO_3^- removal and the best selectivity towards N_2 production in an undivided electrochemical cell are controlled by the combination of the cathodic reduction pathways (k_1 and k_2) and the anodic NH_3 oxidation rate (k_3). Among the studied electrodes, S_2 and S_3 are the most effective for the NO_3^- conversion toward N_2. In S_2, the interplay of the direct NO_3^- to N_2 reduction (k_2) and the anodic NH_3/NH_4^+ oxidation (k_3) retains NH_3/NH_4^+ accumulation and drives the process toward predominant N_2 production within all the applied potentials. S_3 produces significant percentages of N_2 through both cathodic and anodic pathways, especially at higher potentials where k_3 increases. On the other hand, S_1 promotes NH_3/NH_4^+ formation due to the predominant k_1 and mild k_3 and that makes it less suitable for applications that focus on the complete removal of NO_3^-. S_4 has poor activity overall, with slow nitrate reduction kinetics and low selectivity for both N_2 and NH_3/NH_4^+. Finally, the results obtained reveal that boosting N_2 formation from nitrate in an undivided electrochemical cell needs catalysts that enhance the NO_3^- to N_2 reduction pathway while simultaneously promoting rapid oxidation of any intermediate NH_3/NH_4^+. These outcomes highlight the importance of modulating both cathodic and anodic kinetics to reach efficient and selective N_2 production during NO_3RR.

Supplementary Materials: The following supporting information can be downloaded at https://www.mdpi.com/article/10.3390/catal16070651/s1, Figure S1: Current density -time profiles under constant applied potential (E vs. SCE = −1.1 V, −1.3 V, −1.5 V) for samples S_1 (A,B), S_2 (C,D), S_3(E,F) and S_4 (G,H). Current densities are normalised to geometric area and ECSA; Figure S2: Nyquist plot of sample S_3 recorded in 1 M KOH containing 0.1 M KNO_3. Experimental data (symbols) and fitted curves (solid lines) are shown together with the equivalent circuit used for fitting; Table S1: Fitted electrochemical impedance spectroscopy (EIS) parameters for samples S1–S4 obtained using the equivalent circuit reported in Figure S2; Figure S3: Trend with time of experimental (dots) and model predicted data (lines) of nitrate, ammonia and nitrogen concentrations during the electrolysis at E(vs. SCE) = −1.1 V. (A) sample S_1, (B) sample S_2 and (C) sample S_3; Figure S4: Trend with time of experimental (dots) and model predicted data (lines) of nitrate, ammonia and nitrogen concentrations

during the electrolysis at E(vs. SCE) = −1.5V. (A) sample S_1, (B) sample S_2, (C) sample S_3 and (D) sample S_4.

Author Contributions: Conceptualization, A.V. and M.M.; investigation, M.G.R., N.M. and L.M.; writing—original draft, M.G.R., A.V., L.M. and N.M.; writing—review and editing, A.V. and M.M. All authors have read and agreed to the published version of the manuscript.

Funding: This work has been developed as part of the research project RETURN (multi-Risk sciEnce for resilienT commUnities undeR a changiNg climate), funded within the Next Generation EU framework (project code MUR: PE0000005 CUP: F53C22000730002). N.M. gratefully acknowledges the research project NEST (Network 4 Energy Sustainable Transition, project code MUR PE0000021) for funding his fellowship. M.G.R. gratefully acknowledges the Italian National Agency for New Technologies, Energy and Sustainable Economic Development ENEA (CUP: F87G2600003005) for funding his fellowship.

Data Availability Statement: Data is contained within the article.

Conflicts of Interest: The authors declare no conflicts of interest.

Abbreviations

The following abbreviations are used in this manuscript:

MAP	Magnesium ammonium phosphate hexahydrate
EC	Electrochemical reduction
NO_3RR	Electrochemical nitrate reduction reaction
NO_2^-	Nitrite
NO	Nitric oxide
N_2O	Nitrous oxide
NH_2OH	Hydroxylamine
NH_3	Ammonia
N_2	dinitrogen
ECSA	electrochemical active surface area
SEM	scanning electron microscopy
EDX	Energy dispersive X-ray
PED	Pulsed electrodeposition
DE	Direct electrodeposition
ND	Nickel disk
NF	Nickel foam
NiMn-LDH	Nickel-manganese layered double hydroxide
C_{tot}	Total capacitance
C_{DL}	Double-layer capacitance
C_{diff}	Diffusion-related capacitance
ESEM	Environmental scanning electron microscopy

References

1. Zhou, Y.; Zhu, Y.; Zhu, J.; Li, C.; Chen, G. A Comprehensive Review on Wastewater Nitrogen Removal and Its Recovery Processes. *Int. J. Environ. Res. Public Health* **2023**, *20*, 3429. [CrossRef] [PubMed]
2. Ullah, S.; Wang, S.; Li, C.; Ullah Jan, A.; Zhan, F.; Sharif, H.M.A.; Liu, Q.; Wang, G. Recent Developments in Designing Cu-Based Electrocatalysts and Advanced Strategies for Electrochemical Nitrate Reduction to Ammonia. *J. Environ. Chem. Eng.* **2023**, *11*, 110927. [CrossRef]
3. Lu, X.; Song, H.; Cai, J.; Lu, S. Recent Development of Electrochemical Nitrate Reduction to Ammonia: A Mini Review. *Electrochem. Commun.* **2021**, *129*, 107094. [CrossRef]
4. Wu, Y.; Lu, K.K.; Xu, L.H. Progress and Prospects of Electrochemical Reduction of Nitrate to Restore the Nitrogen Cycle. *J. Mater. Chem. A Mater.* **2023**, *11*, 17392–17417. [CrossRef]
5. Zeng, Y.; Priest, C.; Wang, G.; Wu, G. Restoring the Nitrogen Cycle by Electrochemical Reduction of Nitrate: Progress and Prospects. *Small Methods* **2020**, *4*, 2000672. [CrossRef]

6. Veerathangam, K.; Nancy Anna Anasthasiya, A.; Liu, Y.; Yin, J.; Phiri, P.; Li, Y.; Yu, J.; Cheng, Y.; Liu, N.; Xu, L.; et al. Rational Design on Cu-Based Electrochemical Catalyst for Efficient Green Ammonia Production from Nitrate: A Review. *J. Environ. Chem. Eng.* **2025**, *13*, 117055. [CrossRef]
7. Moon, Y.H.; Kim, N.Y.; Kim, S.M.; Jang, Y.J. Recent Advances in Electrochemical Nitrogen Reduction Reaction to Ammonia from the Catalyst to the System. *Catalysts* **2022**, *12*, 1015. [CrossRef]
8. Chen, J.G.; Crooks, R.M.; Seefeldt, L.C.; Bren, K.L.; Morris Bullock, R.; Darensbourg, M.Y.; Holland, P.L.; Hoffman, B.; Janik, M.J.; Jones, A.K.; et al. Beyond Fossil Fuel–Driven Nitrogen Transformations. *Science* **2018**, *360*, eaar6611. [CrossRef] [PubMed]
9. Garcia-Segura, S.; Lanzarini-Lopes, M.; Hristovski, K.; Westerhoff, P. Electrocatalytic Reduction of Nitrate: Fundamentals to Full-Scale Water Treatment Applications. *Appl. Catal. B* **2018**, *236*, 546–568. [CrossRef]
10. Meng, S.; Ling, Y.; Yang, M.; Zhao, X.; Osman, A.I.; Al-Muhtaseb, A.H.; Rooney, D.W.; Yap, P.S. Recent research Progress of Electrocatalytic Reduction Technology for Nitrate Wastewater: A Review. *J. Environ. Chem. Eng.* **2023**, *11*, 109418. [CrossRef]
11. Fu, X.-X.; Guo, H.; Si, D.-H.; Zhu, H.-J.; Lan, Y.-Y.; Huang, Y.-B.; Cao, R. Hydrogen-Bond Mediated Electrocatalytic Nitrate Reduction to Ammonia over Metal–Organic Frameworks with Industrial Current Density. *Chem. Sci.* **2025**, *16*, 13503–13513. [CrossRef] [PubMed]
12. Yin, S.; Wang, Y. Progress and Challenges in the Electrocatalytic Reduction of Nitrate to Ammonia. *Molecules* **2025**, *30*, 3910. [CrossRef] [PubMed]
13. Lin, C.; Lai, C.; Chen, P. Recent Advances in Atomically Engineered Catalysts for Sustainable Ammonia Electrosynthesis. *J. Energy Chem.* **2026**, *119*, 675–694. [CrossRef]
14. Dai, R.; Chen, P. Advances in Co-Based Electrocatalysts for Sustainable Ammonia Synthesis: Mechanisms, Design Strategies, and Emerging Applications. *Mater. Horiz.* **2026**, *13*, 2127–2151. [CrossRef] [PubMed]
15. Zhao, Z.; Nian, Y.; Shi, J.; Xin, X.; Huang, X.; Shi, Y.; Tan, J.; Zhang, Y.; Han, Y.; Yang, D.; et al. Engineering Reaction Pathway to Harmonize the Competition between NRR and HER for Efficient Photocatalytic Ammonia Synthesis. *ACS Catal.* **2024**, *14*, 11626–11634. [CrossRef]
16. Choi, C.; Gu, G.H.; Noh, J.; Park, H.S.; Jung, Y. Understanding Potential-Dependent Competition between Electrocatalytic Dinitrogen and Proton Reduction Reactions. *Nat. Commun.* **2021**, *12*, 4353. [CrossRef] [PubMed]
17. Wu, T.; Melander, M.M.; Honkala, K. Coadsorption of NRR and HER Intermediates Determines the Performance of Ru-N4 toward Electrocatalytic N2 Reduction. *ACS Catal.* **2022**, *12*, 2505–2512. [CrossRef]
18. Santos, A.S.G.G.; Restivo, J.; Orge, C.A.; Pereira, M.F.R.; Soares, O.S.G.P. Nitrate Catalytic Reduction over Bimetallic Catalysts: Catalyst Optimization. *C* **2020**, *6*, 78. [CrossRef]
19. Niu, S. Recent Progress and Challenges in Structural Construction Strategy of Metal-Based Catalysts for Nitrate Electroreduction to Ammonia. *J. Energy Chem.* **2023**, *86*, 69–83. [CrossRef]
20. Wang, Z.; Young, S.D.; Goldsmith, B.R.; Singh, N. Increasing Electrocatalytic Nitrate Reduction Activity by Controlling Adsorption through PtRu Alloying. *J. Catal.* **2021**, *395*, 143–154. [CrossRef]
21. Zhang, Z.; Zhang, N.; Zhang, J.; Deng, B.; Cao, Z.; Wang, Z.; Wei, G.; Zhang, Q.; Jia, R.; Xiang, P.; et al. Critical Review in Electrocatalytic Nitrate Reduction to Ammonia towards a Sustainable Nitrogen Utilization. *Chem. Eng.* **2024**, *483*, 148952. [CrossRef]
22. Rao, T.; Chen, Y.; Hong, Y.; Yu, F.; Zhang, L.-H. Boosting Electrochemical Nitrate Reduction Over a Wide Concentration Range through Constructing Bidirectional Electron Transfer Channels. *ACS Appl. Mater. Interfaces* **2025**, *17*, 37918–37926. [CrossRef] [PubMed]
23. Duan, W.; Li, Y.; Ou, Y.; Tuo, H.; Tian, L.; Zhu, Y.; Fu, H.; Zheng, W.; Feng, C. Insights into Electrochemical Nitrate Reduction to Nitrogen on Metal Catalysts for Wastewater Treatment. *Environ. Sci. Technol.* **2025**, *59*, 3263–3275. [CrossRef] [PubMed]
24. Li, Y.; Bai, Y.; Wang, Y.; Lu, S.; Fang, L. Precise Structural Regulation of Copper-Based Electrocatalysts for Sustainable Nitrate Reduction to Ammonia. *Environ. Res.* **2025**, *266*, 120422. [CrossRef] [PubMed]
25. Karamad, M.; Goncalves, T.J.; Jimenez-Villegas, S.; Gates, I.D.; Siahrostami, S. Why Copper Catalyzes Electrochemical Reduction of Nitrate to Ammonia. *Faraday Discuss.* **2022**, *243*, 502–519. [CrossRef] [PubMed]
26. Mattarozzi, L.; Cattarin, S.; Comisso, N.; Guerriero, P.; Musiani, M.; Vázquez-Gómez, L.; Verlato, E. Electrochemical Reduction of Nitrate and Nitrite in Alkaline Media at CuNi Alloy Electrodes. *Electrochim. Acta* **2013**, *89*, 488–496. [CrossRef]
27. Mattarozzi, L.; Cattarin, S.; Comisso, N.; Gambirasi, A.; Guerriero, P.; Musiani, M.; Vázquez-Gómez, L.; Verlato, E. Hydrogen Evolution Assisted Electrodeposition of Porous Cu-Ni Alloy Electrodes and Their Use for Nitrate Reduction in Alkali. *Electrochim. Acta* **2014**, *140*, 337–344. [CrossRef]
28. Qu, Y.; Li, X.; Xia, Y.; Lan, H.; Ding, L.; Zhong, J.; Chang, X. Enhanced Nitrate Reduction to Ammonia Using Cu-Ni Catalyst: Synergistic Mechanisms and Reaction Pathways. *J. Environ. Sci.* **2026**, *159*, 23–32. [CrossRef] [PubMed]
29. Zhu, H.; Tang, Y.; Wang, J.J.; Sun, T.; Wang, M.; Wang, J.; Tan, Y.; Wang, J. Accelerating Electrosynthesis of Ammonia from Nitrates Using Coupled NiO/Cu Nanocomposites. *Chem. Comm.* **2024**, *60*, 2184–2187. [CrossRef] [PubMed]

30. Su, L.; Han, D.; Zhu, G.; Xu, H.; Luo, W.; Wang, L.; Jiang, W.; Dong, A.; Yang, J. Tailoring the Assembly of Iron Nanoparticles in Carbon Microspheres toward High-Performance Electrocatalytic Denitrification. *Nano Lett.* **2019**, *19*, 5423–5430. [CrossRef] [PubMed]
31. Zhang, F.; Luo, J.; Chen, J.; Luo, H.; Jiang, M.; Yang, C.; Zhang, H.; Chen, J.; Dong, A.; Yang, J. Interfacial Assembly of Nanocrystals on Nanofibers with Strong Interaction for Electrocatalytic Nitrate Reduction. *Angew. Chem. Int. Ed.* **2023**, *62*, e202310383. [CrossRef] [PubMed]
32. Durivault, L.; Brylev, O.; Reyter, D.; Sarrazin, M.; Bélanger, D.; Roué, L. Cu-Ni Materials Prepared by Mechanical Milling: Their Properties and Electrocatalytic Activity towards Nitrate Reduction in Alkaline Medium. *J. Alloys Compd.* **2007**, *432*, 323–332. [CrossRef]
33. Hao, M.; Charbonneau, V.; Fomena, N.N.; Gaudet, J.; Bruce, D.R.; Garbarino, S.; Harrington, D.A.; Guay, D. Hydrogen Bubble Templating of Fractal Ni Catalysts for Water Oxidation in Alkaline Media. *ACS Appl. Energy Mater.* **2019**, *2*, 5734–5743. [CrossRef]
34. Sengupta, S.; Patra, A.; Jena, S.; Das, K.; Das, S. A Study on the Effect of Electrodeposition Parameters on the Morphology of Porous Nickel Electrodeposits. *Metall. Mater. Trans. A Phys. Metall. Mater. Sci.* **2018**, *49*, 920–937. [CrossRef]
35. Jituri, S.D.; Nikam, S.M.; Bane, T.S.; Inamdar, A.I.; Mujawar, S.H. Porous Cauliflower-like Nanoarchitectures of NiMn-Layered Double Hydroxide as a Promising Electrode for Oxygen Evolution Reaction and Supercapacitor Applications. *Electrochim. Acta* **2025**, *513*, 145544. [CrossRef]
36. Wang, X.; Jiang, M.; Yang, P.; Zhou, H.; Xi, W.; Duan, J.; Ratova, M.; Wu, D.; Jiang, X. Recent Advances in Pulsed Electrochemical Techniques: Synthesis of Electrode Materials and Electrocatalytic Reactions. *Surf. Interfaces* **2024**, *50*, 104519. [CrossRef]
37. Wang, X.; Ma, X.; Wu, Y.; Li, C.; Chen, R. Electrocatalytic Nitrate Removal by Non-Precious Three-Dimensional Fe/Ni Foam Cathode: Experimental Study and Mechanism Verification. *J. Water Process Eng.* **2024**, *64*, 105590. [CrossRef]
38. Yu, X.; Yang, J.; Sui, Z.; Wang, M. Effects of Ultrasonic Field on Structure Evolution of Ni Film Electrodeposited by Bubble Template Method for Hydrogen Evolution Electrocatalysis. *J. Solid State Electrochem.* **2021**, *25*, 2201–2212. [CrossRef]
39. Eugénio, S.; Silva, T.M.; Carmezim, M.J.; Duarte, R.G.; Montemor, M.F. Electrodeposition and Characterization of Nickel-Copper Metallic Foams for Application as Electrodes for Supercapacitors. *J. Appl. Electrochem.* **2014**, *44*, 455–465.
40. Santos, D.M.F.; Eugenio, S.; Sequeira, C.A.C.; Montemor, M.F. Transition Metal Foam Electrocatalysts for Hydrogen Evolution Reaction. *ECS Trans.* **2015**, *64*, 9–16. [CrossRef]
41. Liu, J.; Zhou, Y.; Xie, Z.; Li, Y.; Liu, Y.; Sun, J.; Ma, Y.; Terasaki, O.; Chen, L. Conjugated Copper–Catecholate Framework Electrodes for Efficient Energy Storage. *Angew. Chem.* **2020**, *132*, 1097–1102. [CrossRef]
42. Ardizzone, S.; Fregonara, G.; Trasatti, S. "Inner" and"outer" activesurface of RuO electrodes. *Electrochim. Acta* **1990**, *35*, 263–267. [CrossRef]
43. Zarach, Z.; Szkoda, M.; Trzciński, K.; Łapiński, M.; Trykowski, G.; Nowak, A.P. The Phenomenon of Increasing Capacitance Induced by 1T/2H-MoS2 Surface Modification with Pt Particles—Influence on Composition and Energy Storage Mechanism. *Electrochim. Acta* **2022**, *435*, 141389. [CrossRef]
44. Duay, J.; Sherrill, S.A.; Gui, Z.; Gillette, E.; Lee, S.B. Self-Limiting Electrodeposition of Hierarchical MnO2 and M(OH)2/MnO2 Nanofibril/Nanowires: Mechanism and Supercapacitor Properties. *ACS Nano* **2013**, *7*, 1200–1214. [CrossRef] [PubMed]
45. Mais, L.; Palmas, S.; Mascia, M.; Sechi, E.; Casula, M.F.; Rodriguez, J.; Vacca, A. Porous Ni Photocathodes Obtained by Selective Corrosion of Ni-Cu Films: Synthesis and Photoelectrochemical Characterization. *Catalysts* **2019**, *9*, 453. [CrossRef]
46. Xu, H.; Ma, Y.; Chen, J.; Zhang, W.X.; Yang, J. Electrocatalytic Reduction of Nitrate—A Step towards a Sustainable Nitrogen Cycle. *Chem. Soc. Rev.* **2022**, *51*, 2710–2758. [CrossRef] [PubMed]
47. Luo, W.; Guo, Z.; Ye, L.; Wu, S.; Jiang, Y.; Xu, P.; Wang, H.; Qian, J.; Zhou, X.; Tang, H.; et al. Electrical-Driven Directed-Evolution of Copper Nanowires Catalysts for Efficient Nitrate Reduction to Ammonia. *Small* **2024**, *20*, e2311336. [CrossRef] [PubMed]
48. Zou, Z.; Zhang, H.; Pan, X.; Shen, H.; Yu, J.; Guo, T.; Wang, Y. Role of Electrons and H* in Electrocatalytic Nitrate Reduction to Ammonium for CuNi Alloy. *Surf. Interfaces* **2024**, *54*, 105308. [CrossRef]
49. Zhou, J.; Wen, M.; Huang, R.; Wu, Q.; Luo, Y.; Tian, Y.; Wei, G.; Fu, Y. Regulating Active Hydrogen Adsorbed on Grain Boundary Defects of Nano-Nickel for Boosting Ammonia Electrosynthesis from Nitrate. *Energy Environ. Sci.* **2023**, *16*, 2611–2620. [CrossRef]
50. He, W.; Zhang, J.; Dieckhöfer, S.; Varhade, S.; Brix, A.C.; Lielpetere, A.; Seisel, S.; Junqueira, J.R.C.; Schuhmann, W. Splicing the Active Phases of Copper/Cobalt-Based Catalysts Achieves High-Rate Tandem Electroreduction of Nitrate to Ammonia. *Nat. Commun.* **2022**, *13*, 1129. [CrossRef] [PubMed]
51. Shih, Y.J.; Wu, Z.L.; Huang, Y.H.; Huang, C.P. Electrochemical Nitrate Reduction as Affected by the Crystal Morphology and Facet of Copper Nanoparticles Supported on Nickel Foam Electrodes (Cu/Ni). *Chem. Eng.* **2020**, *383*, 123157. [CrossRef]
52. Augustyn, V.; Simon, P.; Dunn, B. Pseudocapacitive Oxide Materials for High-Rate Electrochemical Energy Storage. *Energy Environ. Sci.* **2014**, *7*, 1597. [CrossRef]
53. Jung, S.; Bae, S.; Lee, W. Development of Pd–Cu/Hematite Catalyst for Selective Nitrate Reduction. *Environ. Sci. Technol.* **2014**, *48*, 9651–9658. [CrossRef] [PubMed]

54. Pérez-Gallent, E.; Figueiredo, M.C.; Katsounaros, I.; Koper, M.T.M. Electrocatalytic Reduction of Nitrate on Copper Single Crystals in Acidic and Alkaline Solutions. *Electrochim. Acta* **2017**, *227*, 77–84. [CrossRef]
55. Tan, X.; Wang, X.; Zhou, T.; Chen, T.; Liu, Y.; Ma, C.; Guo, H.; Li, B. Preparation of Three Dimensional Bimetallic Cu–Ni/NiF Electrodes for Efficient Electrochemical Removal of Nitrate Nitrogen. *Chemosphere* **2022**, *295*, 133929. [CrossRef] [PubMed]
56. Zhang, T.; Shi, K.; Wang, B.; Hou, X. Mechanistic Insights into the Intercorrelation between the Hydrogen Evolution Reaction and Nitrate Reduction to Ammonia: A Review. *ACS Catal.* **2025**, *15*, 9814–9844. [CrossRef]
57. Zhao, Y.; Zhou, X.; Wu, Y.; Wang, W.; Kang, W.; Li, H.; Yu, H. Electrocatalytic Reduction of NO3− in Copper-Supported Charcoal Microchannels for Effective Denitrification. *Chem. Eng.* **2025**, *503*, 158681. [CrossRef]
58. Xiong, Y.; Wang, Y.; Zhou, J.; Liu, F.; Hao, F.; Fan, Z. Electrochemical Nitrate Reduction: Ammonia Synthesis and the Beyond. *Adv. Mater.* **2024**, *36*, e2304021. [CrossRef] [PubMed]
59. Polatides, C.; Kyriacou, G. Electrochemical Reduction of Nitrate Ion on Various Cathodes—Reaction Kinetics on Bronze Cathode. *J. Appl. Electrochem.* **2005**, *35*, 421–427. [CrossRef]
60. Plowman, B.J.; Jones, L.A.; Bhargava, S.K. Building with Bubbles: The Formation of High Surface Area Honeycomb-like Films via Hydrogen Bubble Templated Electrodeposition. *Chem. Commun.* **2015**, *51*, 4331–4346. [CrossRef] [PubMed]